

---

# Multi-Scale Modelling of NC-AFM Imaging and Manipulation at Insulating Surfaces

T. Trevethan, N. Martsinovich, L. Kantorovich, and A.L. Shluger

**Abstract.** We present the results of calculations performed to simulate the process of atomic-scale imaging and manipulation that explicitly take into account dynamical processes occurring at the surface. These calculations are performed using a novel multi-scale method that combines a simulation of the experimental instrument coupled with a kinetic Monte Carlo simulation of the microscopic system that evolves in real time. This method is applied to three qualitatively different systems: the manipulation of a Pd atom adsorbed on the MgO (001) surface, the imaging of the thermally induced motion of a water molecule adsorbed on the CeO<sub>2</sub> (111) surface, and the manipulation of a C<sub>60</sub> molecule on the Si (001) surface. The results of these simulations show how optimum protocols for controlled atomic-scale manipulation can be determined and how dynamical surface processes can significantly affect the contrast seen in NC-AFM images.

## 12.1 Introduction

The interpretation of the results of atomic resolution non-contact atomic-force microscopy experiments is a difficult and challenging task, due to both the complexity of the imaging mechanism and the unknown nature of the exact tip-apex structure [1]. Therefore, it is necessary to employ theoretical modelling to better understand the results produced by a particular experiment. The application of theory to modelling NC-AFM images has been able to explain the contrast patterns observed and identify features in many atomic resolution experiments [1–3] and has proved invaluable to the advance of the field over the past decade. The modelling of an NC-AFM experiment typically involves calculating a tip–surface force-field – for a particular tip and a particular surface – from atomistic simulations. This force-field, which gives the vertical force on the tip as a function of tip position in three-dimensions above the surface, can then be used to calculate the frequency-shift (also as a function of tip position) from the cantilever parameters and the amplitude

by integrating over the tip trajectory [4]. This in turn can then be used to create either a constant height image of frequency or a topography image at a given frequency shift set-point. This procedure, however, involves several important simplifying assumptions. The first of these is that the NC-AFM instrumentation controlling the cantilever oscillations and the surface position act ideally, i.e., that the tip follows a sinusoidal trajectory, and that the lateral scanning speed is slow enough that any finite response of the amplitude or frequency feed-back loops can be neglected; in other words, it is assumed that the instrumentation reacts instantaneously during the scan on the constantly undulating surface. The second assumption is that the tip-experiences a conservative force-field due to its interaction with the surface, and that there are no non-conservative processes i.e., no atomic-scale structural changes occur during the entire imaging process.

In many NC-AFM images of stable and well defined surfaces and systems, the assumptions described earlier are applicable and well tested [1,4,5]. However, there are many instances where this is not the case: e.g., when microscopic structural changes occur to the surface or tip during the imaging process. These structural changes may consist of the thermally driven diffusion of an adsorbate across a surface, or may be induced by the tip at close approach – something that is produced intentionally in an atomic-scale manipulation experiment [6–8]. When considering the effect of dynamical processes during the experiment, the interpretation and modelling becomes significantly more complex and challenging.

To understand the effect of various dynamical processes during an NC-AFM experiment, it is useful to consider the various time-scales involved. The chemical force that acts between the tip and the surface at close approach is sensitive to the thermal vibrations of individual atoms in both the surface and the tip, which typically have a characteristic frequency of  $10^{12}$ – $10^{14}$  Hz. The cantilever, however, oscillates with a frequency on the order of  $10^5$  Hz, and so atoms in the junction will vibrate billions of times over a single oscillation of the tip. It has been shown earlier that the force fluctuations of these fast lattice vibrations are effectively averaged over the tip trajectory, and the tip “feels” the system in its ground state configuration (within the harmonic approximation) resulting in a conservative tip–surface interaction [9,10]. Other processes that result in structural changes, may occur over a vast range of time-scales: rare hops and manipulation events may occur only a few times during the acquisition of an entire image (which occurs over the order of seconds to minutes) resulting in definite changes in contrast as the image is scanned. Faster diffusion processes may occur at a frequency comparable to the tip oscillations, and in this case the response of the instrument and the interplay between the diffusion and tip oscillations is difficult to predict. In all cases, the dynamical evolution of the surface processes and the motion of the tip are not independent of one another, but directly coupled and must be treated as a single interacting system.

In this contribution we explain how an explicit, real-time and multi-scale simulation of the entire NC-AFM experiment, including the dynamical evolution of the instrumentation at the macroscopic scale and atomistic processes at the microscopic scale, can help in understanding the imaging of complex process and how atomic- and molecular-scale manipulation can best be achieved and detected. Modelling the imaging process requires spanning both the time of acquiring an entire image and the characteristic time-scale of atomic-scale transitions – a complex task that requires the use of novel methods.

We apply this model to three realistic but qualitatively different systems: the manipulation and diffusion of a Pd adatom on the MgO (001) surface, the thermally induced structural change of an H<sub>2</sub>O molecule on the CeO<sub>2</sub> surface and the manipulation of a C<sub>60</sub> molecule on the Si (001) surface. In the first system, which consists of a metal adatom weakly bound to an ionic surface, we model how the atom can be manipulated at close approach and also the image contrast when the atom is freely diffusing across the surface. In the second system, we image the fast structural changes of a small molecule that is strongly bound and immobile on the surface but free to move between three equivalent states. In the final example, we model the manipulation by the tip of a much larger molecule that is strongly bound to the surface.

Section 12.2 outlines the details of the model and how this is implemented in the simulation. Section 12.3 then describes the application of the model to the three example systems. In Sect. 12.4 a discussion is given.

## 12.2 Methods

The simulation of the NC-AFM experiment is treated in two separate parts: the instrument and the microscopic system. These are then linked together to form a complete self-consistent simulation.

### 12.2.1 Modelling the Instrument

The NC-AFM instrumentation controls the amplitude of the cantilever oscillations and the position of the surface (and hence the frequency shift) with two feed-back loops: the automatic gain control (AGC) and the automatic distance control (ADC), respectively (see Fig. 12.1). These loops are implemented using a complex set-up of electronics, incorporating a digital phase locked loop as a frequency demodulator, and a laser diode detection system to measure the deflection of the cantilever [4]. The instrument outputs three signals that can be used for generating images: the sample height (topography), the frequency shift (detuning) and the excitation signal (dissipation).

To model the complex behaviour of this instrument we employ a Virtual atomic-force microscope (VAFM), which consists of an explicit numerical simulation of the entire experiment in real time, and is described in detail in [11, 12]. The VAFM, we employ, performs a numerical integration of the

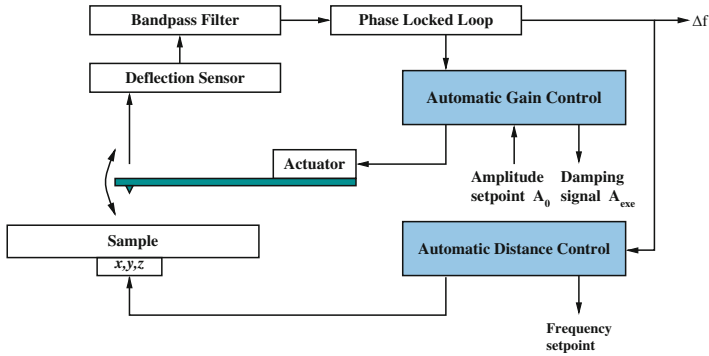


Fig. 12.1. Block diagram showing the interacting parts of the virtual AFM

trajectory of the cantilever, the control electronics and the driving signal with a fixed time-step, which is small compared with the motion of the tip (approximately  $10^{-10}$  s). The tip moves in a three-dimensional force-field above the surface as the tip is oscillated and the surface is scanned. The scanning of the surface takes place continuously and the oscillating tip follows a lateral path collecting line scans to produce an image, in real time. The lateral trajectory in the calculations presented here consists of a raster scan without flyback – with the surface moving alternately in perpendicular fast and slow directions to build up all the lines for the complete image. Other implementations of dynamic AFM instrument simulations can be found in [13, 14].

By performing a complete real-time simulation of the instrument, the force-field experienced by the tip can be altered to reflect a structural change in the surface during the imaging process. The simulations including the trajectory of the tip, all the control mechanisms and the output signals, will react in a completely realistic way as the experiment progresses.

### 12.2.2 Modelling the Tip–Surface Junction

At the heart of all calculations to model NC-AFM experiments is the tip–surface force-field, which usually consists of two components: a macroscopic van der Waals force, which depends only on the tip–surface separation and a microscopic force-field which is sensitive to the atomic-scale structure of the surface and tip. The microscopic force-field depends strongly on the exact chemical nature and structure of the tip model used, and so the choice of this tip model is critical to the outcome of a simulation and the predicted contrast. The exact nature of the tip-apex used in the actual experiment is unknown: tips are usually fabricated from silicon, but are exposed to the atmosphere and so form an oxide layer and may be contaminated with other species. In addition the tip is most likely to be contaminated by material from the surface under investigation during the experiment.

The identity of the tip-apex can be determined by simulating an NC-AFM image with many different types of tips and selecting the tip that gives the closest match to the observed contrast pattern [15, 16]. In addition, force-curves over individual surface atoms can be determined from force-spectroscopy experiments and further used to characterize the tip-surface interaction [17, 18]. However, to reach a qualitative understanding of the imaging process, model tips are often employed which significantly reduce the computational effort involved in calculating tip-surface interactions.

With a given tip model, the force-field can be calculated from a series of atomistic calculations. With the tip in a fixed position above the surface, the force on the tip is calculated after all free atoms in the tip-surface junction are relaxed. This is then repeated for an array of tip positions to obtain the force-field in three dimensions. The method used to calculate the tip force depends on the identity of the surface and the tip model: ideally an ab-initio method, such as density functional theory is employed [19–21]. However, depending on the system, high quality interatomic potentials can be used instead which drastically reduces the computational effort involved by several orders of magnitude. If the microscopic system retains the same structure throughout the experiment, a single force-field is required to model the imaging process. However, structural changes will change the force-field experienced by the tip during the experiment. In this case, a force-field for each structure that is accessible during the simulation is required.

Dynamical processes in the surface and the structural changes associated with them occur from transitions between minima on the potential energy surface (PES) of the tip-surface junction. These transitions (or jumps) are thermally induced and occur when the system crosses a potential energy barrier (or saddle point). Energy barriers for processes in the microscopic system can be calculated from atomistic calculations, employing the same methods used for calculating the force-field.

In many microscopic processes, such as e.g., atomic self-diffusion, the barriers, and hence the rates of transitions, remain constant. However, when the tip of an SPM is interacting with the surface, these barriers can be modified and will change as the tip is moved above the surface. This results in a PES that is a function of tip-position – giving rise to a potential energy barrier field. A “barrier field” then gives the activation energy for a certain process as a function of tip position. The presence of the tip may act to change the barrier for a process at close approach. In fact, as the tip moves in time (both due to vertical oscillations and the lateral scan), the “barrier field” becomes an explicit function of time as well. Manipulation occurs when a barrier that is insurmountable when the tip is far from the surface (and no transitions occur at a given temperature) is lowered by the presence of the tip, allowing a transition to proceed.

The frequency at which atomic-scale transitions occur in the system may be comparable to the tip motion, but the actual transition itself occurs on the time-scale of atomic relaxation (i.e.,  $10^{-12}$  s) i.e., effectively instantaneously

with respect to the tip motion. So, as far as the NC-AFM experiment is concerned, the dynamics of the individual transition is irrelevant – we are only interested in evaluating when they occur. Atomic-scale transitions are an inherently stochastic process that can be modelled realistically using a kinetic Monte Carlo (KMC) method [22], if the rates of the relevant transitions are known.

### 12.2.3 Kinetic Monte Carlo

Given the activation barrier (for a given tip position  $x, y, z$ ), the transition rate for a particular process,  $k$ , can be calculated from the familiar Vineyard expression [23]:

$$r^k(x, y, z) = \nu^k e^{-\beta \Delta E^k(x, y, z)}, \quad (12.1)$$

where  $\nu$  is the attempt pre-factor,  $E^k(x, y, z)$  the energy barrier field for process  $k$  and  $\beta = 1/k_B T$ . In the traditional KMC method, the rates for individual processes are constant and do not change in time [24]. Then, the simulation of the system dynamics is done by, firstly, choosing at random the time-step using the total rate of all possible “positive” processes, and, secondly, choosing, again at random, the particular process from the available list of processes which will take the system to the next state. The standard KMC algorithm is based on considering only “positive” processes which lead to the system changing its state.

To evaluate the dynamics of a system when the barriers (and rates) vary in time due to the motion of the tip, a more general KMC algorithm that employs a fixed time-step  $\Delta t$  must be employed [22]. In this method, a complete set of processes is considered including the one in which nothing happens, i.e., the system remains in its current state (see for example state A in Fig. 12.2b). Then, one considers the probability,  $P_0(\Delta t)$ , for the system to remain in the current state over the time  $\Delta t$  (which exponentially decays with increase of the time step), and the probabilities  $P_k(\Delta t)$ , to move to every available other state  $k$  over the same time (for example the four B states in Fig. 12.2b). By considering the complete system of possible states the system may jump into (including multiple jump events), one ensures that all probabilities add up to unity exactly, i.e.,

$$P_0(\Delta t) + \sum_k P_k(\Delta t) = 1. \quad (12.2)$$

A single random number is drawn to decide which particular state of all available states will be realized, including the remaining in the current state. To avoid complex calculations of all possible paths to reach available states from the current one over the finite time  $\Delta t$  (which should include also jumping to these states via intermediate states, i.e., multiple jump events), one can choose a very small time-step and simply disregard multiple events, in which

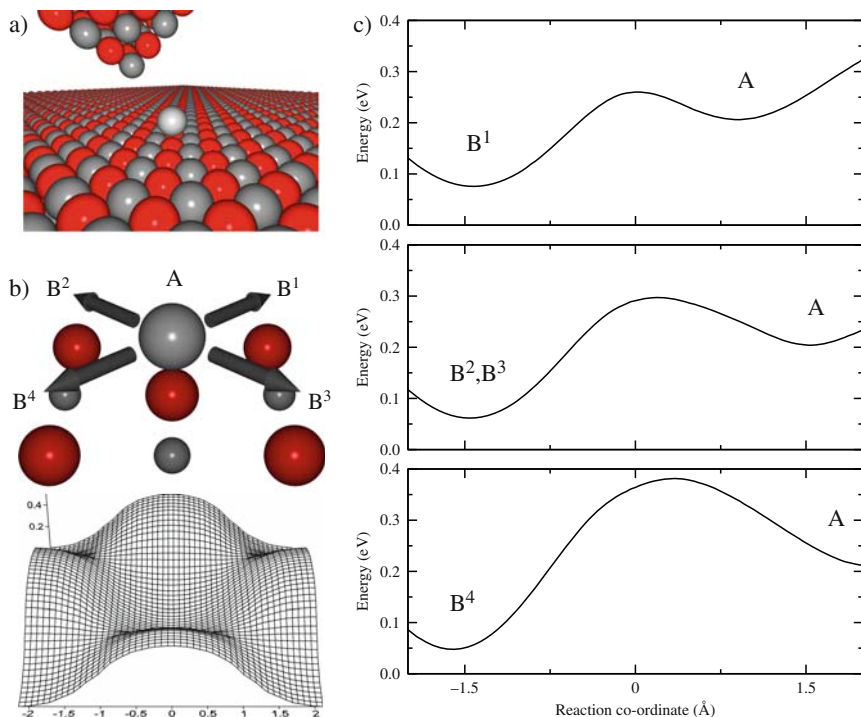


**Fig. 12.2.** (a) Configuration of the surface, adatom and tip (b) *Top*: Schematic of a single oxygen unit cell on the MgO (001) surface with the Pd atom adsorbed above the central O, showing the four equivalent transitions to neighboring oxygen sites. *Bottom*: 2-D potential energy surface for the Pd atom as a function of lateral position above the unit cell. The centre of the cell is located at lateral position  $x = 0$   $y = 0$  and B<sup>1</sup> at  $x = 2.122$  and  $y = 2.122$ . (c) Minimum energy paths along the four reaction coordinates for the Pd atom to move into each of the four neighboring minima with the Mg terminated MgO tip at a height of  $z = 4.5$  Å and lateral position  $x = -0.53$  Å  $y = -0.53$  Å relative to the central O position

case the construction of the possible list of events is trivial. In the case of simulations of AFM induced diffusion of atoms on the surface, we can simply consider single jumps to all nearest lattice sites (e.g., see Fig. 12.2b).

For the given tip position the probabilities of these events can be explicitly calculated given the known energy barriers as functions of the tip position, and the known time step,  $\Delta t$ . Then, a random number is drawn to choose the particular process from the list, i.e., which atom to move and to which lattice site, or to keep the current configuration of the atoms on the surface unchanged (i.e., “do nothing”). Then, as the tip moves over the time  $\Delta t$ , the list of processes is compiled again, their probabilities are recalculated and it is decided what is the next state of the system. Thus, in this algorithm, for a given time-step in the simulation, the probability of the system crossing a

barrier is calculated based on the instantaneous rate, and a random number is drawn to determine whether the barrier is crossed or not.

The KMC simulation is run simultaneously with the VAFM calculation, with the potential energy barrier fields evolving in real time as the tip moves and the surface is imaged. This means the position and motion of the tip alters the dynamics of the surface processes. When a microscopic transition occurs the force-field will switch instantaneously to the corresponding new microscopic structure. In this way both the microscopic and macroscopic parts of the system evolve in-step and self-consistently.

## 12.3 Applications

### 12.3.1 Pd Adatom on MgO (001)

The adsorption and diffusive behaviour of individual Pd atoms and Pd clusters on the MgO (001) surface has been widely studied, with a variety of techniques, primarily as this system is an important catalyst [25]. However, as an example of a system consisting of adatoms weakly bound to an ionic surface, it is useful as model system to investigate the manipulation of individual atoms on an insulator. MgO has the rock-salt structure and the (001) surface is very stable and nearly flat. To model this system, we have employed a set of classical pair-wise inter-atomic potentials that have been derived from high-quality ab-initio calculations of the Pd/MgO interface [26]. The atomistic calculations have been performed using the SciFi code which has been specifically developed to model SPM tip-surface interactions [27].

A single Pd atom is adsorbed directly above the oxygen site on the MgO surface with an adsorption energy of approximately 1 eV. The Pd atom can diffuse on the surface via a nearest neighbor hopping mechanism, and the energy barrier to move to a neighbouring minimum (above a neighboring oxygen) is approximately 0.25 eV and will therefore be highly mobile at room temperature, but immobile at low temperatures (70 K being a convenient reference point). Figure 12.2a shows the configuration of an adsorbed Pd atom on the surface, along with the potential energy surface of this system as a function of the lateral position of the Pd atom (Fig. 12.2b). Here, it is clear that the Pd atom can move in one of four equivalent directions in a single transition. In the description that follows the initial adsorbed position of the Pd atom is labelled state A, and the four neighboring states B<sup>1</sup>, B<sup>2</sup>, B<sup>3</sup>, and B<sup>4</sup>.

It is apparent that the states B<sup>1</sup>, B<sup>2</sup>, B<sup>3</sup>, and B<sup>4</sup> are equivalent, however when a tip is introduced to the system above the surface this symmetry may be broken and the barriers to move into the different states change. This is at the heart of the manipulation mechanism the potential energy surface of the system and hence the individual barriers are modified through the interaction with the tip. In the calculations presented here, the tip is represented by a 64 atom MgO cube oriented so that its threefold axis is perpendicular to the

surface plane and is terminated with a single Mg atom. The upper 32 atoms are frozen in bulk-like positions and the remaining atoms free to relax. This tip is chosen as a convenient model, however the MgO tip has been shown to be representative of a wide variety of polar tips [1]. The nature of the tip apex is crucial to the manipulation mechanism in this case: the Mg apex has a very weak attractive interaction with the Pd adatom (much weaker than the Pd–O interaction), and is therefore able to exert a force (through Pauli repulsion) to “push” the Pd atom at close approach.

The minimum energy path, and hence barrier, for the Pd atom to move from state A to states B<sup>1</sup>, B<sup>2</sup>, B<sup>3</sup>, and B<sup>4</sup> can then be determined for a given position  $(x, y, z)$  of the tip above the surface, using a constrained minimisation procedure (described in [28]). For example, Fig. 12.2c shows each of the four minimum energy paths when the tip apex is positioned at a height of 4.5 Å above the surface and at a lateral position 0.75 Å in the direction to state B<sup>4</sup> from the position directly above state A. Here, the barrier to move to state B<sup>1</sup> is the smallest and the barrier to move to state B<sup>4</sup> the largest (the barriers to move to states B<sup>2</sup> and B<sup>3</sup> are equivalent due to the symmetry). This calculation is then repeated for a three-dimensional array of fixed positions of the tip above the Pd atom and surface to derive the four separate energy barriers as a function of tip position. The barriers are calculated for a grid of positions with  $18 \times 18$  points laterally over the conventional unit cell and 50 tip heights vertically between 4 and 6 Å (a total of 16,200 points). With this complete grid, each of the four energy barriers can be determined for any arbitrary tip-position in three dimensions above the surface by interpolating between these points using a polynomial interpolation scheme. This results in four “energy barrier fields” – which in addition to the force-field of the system enable the complete description of the dynamical evolution for any arbitrary tip trajectory.

The dynamical evolution of this system can then be determined using the kinetic Monte Carlo algorithm, with rates calculated using a standard attempt pre-factor of  $10^{12}$  Hz. The tip trajectory is controlled using the virtual AFM and the system will react in real time. When a jump of the Pd atom occurs (according to the KMC simulation), both the force-field and barrier-fields are instantaneously shifted to the new position of the Pd atom and the simulation continues. The jump of the atom and, hence, of the force-field occurs instantaneously with respect to the motion of the tip and the instrument will respond to the jump in a completely realistic and self-consistent way.

In the calculations presented here, a finite time-step of  $\Delta t = 10^{-9}$  s is used for both the KMC algorithm and the VAFM trajectory. This is sufficiently large to assume that an atomic jump happens instantaneously. In addition to the atomistic tip–surface force-field, an attractive macroscopic van der Waals force (using a spherical tip model with a radius of 10 nm and a Hamaker constant of 1 eV) is added to replicate a realistic tip–surface interaction. The resonant frequency of the cantilever is  $f_0 = 100$  kHz, the spring constant

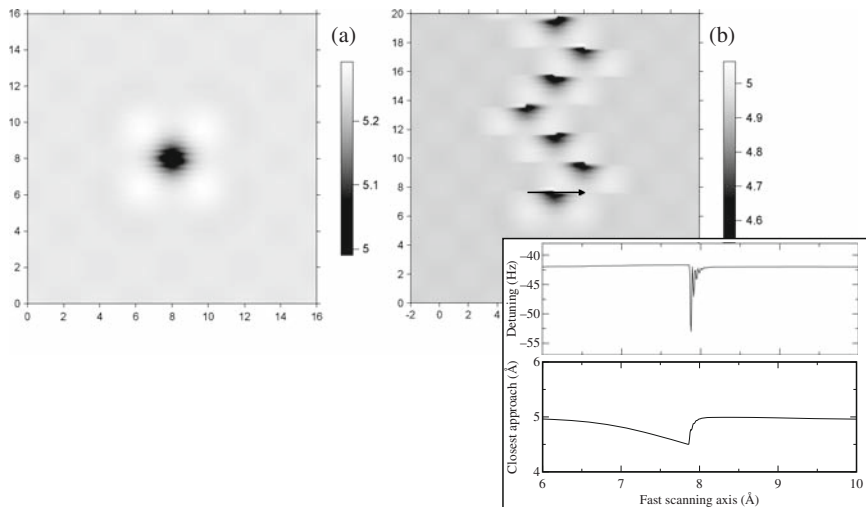


**Fig. 12.3.** (a) Constant frequency shift ( $\Delta f_0 = -38$  Hz) topography image of the Pd atom at the centre of a  $16 \times 16 \text{ \AA}^2$  area of the MgO (001) surface at 10 K. (b) Constant frequency shift ( $\Delta f_0 = -42$  Hz) topography image of the Pd atom on a  $20 \times 20 \text{ \AA}^2$  area of the MgO (001) at 10 K. The frequency detuning along the fast scan line indicated and the corresponding distance of closest approach (topography) are shown as an *inset*

20 N/m and the set-point amplitude  $A_0 = 10$  nm. All the other parameters for the instrument are described in [28].

Figure 12.3a shows a topography scan of a Pd atom on the MgO (001) surface (scan area  $16 \times 16 \text{ \AA}$ ), for the frequency set-point  $\Delta f_0 = -38$  Hz and at 10 K, with the slow scanning direction going from top to bottom. The topography is low (dark) over Pd atom due to the short-range repulsion with the Mg terminated tip; however, the tip is not yet getting close enough to the surface to significantly lower any barrier to induce a jump of the adatom. To illustrate the time-scales involved, this image is acquired over several minutes of real time (although it takes many hours to calculate). Each scan line takes 0.4 s, during which the cantilever will have oscillated approximately 40,000 times over  $4 \times 10^8$  simulation time-steps.

Figure 12.3b shows the same scan, but this time performed at a frequency shift set-point of  $\Delta f_0 = -42$  Hz, which now brings the tip closer to the surface (and Pd atom) at close approach. Now the Pd atom is being pushed upwards as the scan progresses, resulting in the “half moon” shapes as the atom jumps to a neighboring site as a single line is scanned. Figure 12.3b also shows the instantaneous frequency shift (detuning) and topography as a jump occurs on the scan line indicated in the image. Here, when the jump occurs, the force-field changes and the instrument retracts the surface to maintain the set-point frequency shift, which happens over a finite time due to the response of the

instrument [29]. In an ideal instrument, the frequency shift would remain constant, however, in reality a spike occurs due to the instantaneous jump. This strong response signature can be used as a confirmation of successful manipulation and to identify the exact point a manipulation occurs. In addition, the jump of the atom (and force-field) will cause a difference in the tip–surface force during the approach and retraction over a single oscillation cycle that will lead to a spike in the dissipation (amplitude gain) signal, however in this case the effect is small (a peak of 5 meV) and is unlikely to be detected in a real experiment.

With this simulation it is now possible to determine the outcomes and success of various manipulation protocols, which can be used to guide experimental efforts. For example, it is the case that scanning in the (110) direction offers less control over the Pd atom (i.e., more uncertainty in the direction of manipulation) than scanning in the (100) direction [28]. However, both of these protocols demonstrate only limited control over the adatom and are also sensitive to the direction of the scanning. The lack of control is due to the fact that during *scanning* the tip on its trajectory visits regions that will cause the manipulation in several different directions, only one of which is *desired*.

An alternative is to position the tip only in a “high success” region along a predetermined trajectory [29], through a vertical approach of the oscillating cantilever over a fixed lateral position to induce the manipulation in a specific direction. To achieve a high degree of control it is necessary to determine the “high success” manipulation regions from a series of simulations. Here, the probability of the system moving in a particular direction can be determined by repeating the evaluation of a given trajectory of the tip many times to build up statistics.

This manipulation procedure was simulated with the oscillating cantilever approaching the surface with a constant velocity of  $v = 20 \text{ nm s}^{-1}$  up to a distance of closest approach of  $4 \text{ \AA}$ . The final state of the system (either A, B<sup>1</sup>, B<sup>2</sup>, B<sup>3</sup>, or B<sup>4</sup>) is recorded after the approach, and this is repeated 1,000 times. These calculations are then repeated for a grid of lateral positions over the oxygen unit cell shown in Fig. 12.2 (with the Pd atom at the centre) and the proportion of attempts resulting in each state was used to determine the corresponding probabilities.

Figure 12.4 shows lateral plots of probabilities for the protocol described, for temperatures  $T = 10$  and  $70 \text{ K}$ , for achieving the manipulation in a specified direction (here, to state B<sup>2</sup>) and also for manipulating the atom into one of the other three states. The lateral area for achieving a desired manipulation into the B<sup>2</sup> state is on the opposite side to the adatom (as is expected, from a “pushing” mechanism). The area for complete certainty of achieving the desired manipulation to B<sup>2</sup> (and not to any other state) is significantly larger at a lower temperature – showing that a lower system temperature will lead to greater degree of control with this protocol. As is the case with lateral scanning, when the atom jumps, the sudden change in force-field will cause

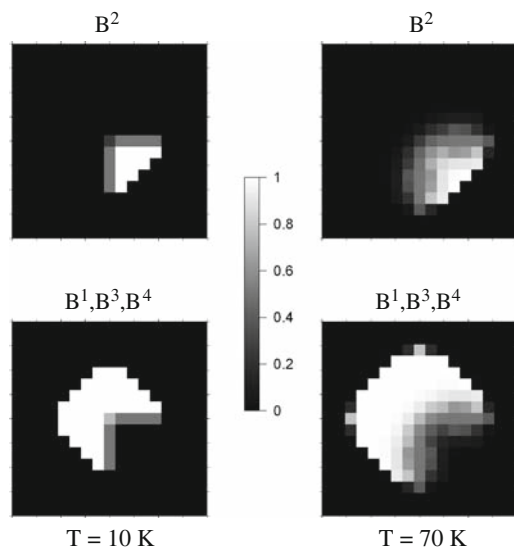


**Fig. 12.4.** Probabilities of manipulating the Pd adatom in different directions, for a constant velocity approach of the oscillating cantilever over a fixed lateral position (on a grid over the oxygen unit cell, where the Pd adatom is initially located in the centre of the cell) for temperatures of 10 and 70 K

a spike in the frequency shift – a signature that can be used to confirm the manipulation has occurred [29].

In the examples of different manipulation protocols earlier, at low temperatures, there are no spontaneous transitions when the tip is far from the surface, i.e., structural changes must be induced by the tip. At higher temperatures, this is no longer the case and the Pd atom may diffuse across the surface as it is scanned. Figure 12.5a shows a constant height (frequency shift) image of the same surface area at a temperature of 110 K, where the rate for a spontaneous jump of the Pd atom is approximately 20 Hz. Here, the atom is jumping between states several times during a single line-scan (even when the tip is not modifying the energy barriers) resulting in bright and dark “stripes” that pattern the image. In this case, the length of a stripe will be proportional to the residence time of the atom. The distribution of the lengths of the different stripes should reveal the average rate for the different processes for different relative positions of the tip and Pd atom.

Figure 12.5b shows an image of the same scan, but this time at a temperature of 180 K. In this image the underlying MgO lattice is visible but with “noise” concentrated over the oxygen sites. In this case, the Pd atom is diffusing on the surface very rapidly, with the rate for a spontaneous transition at 6 MHz which corresponds to an average of 60 jumps over a single oscillation of the cantilever. Figure 12.5c shows the corresponding dissipation (amplitude

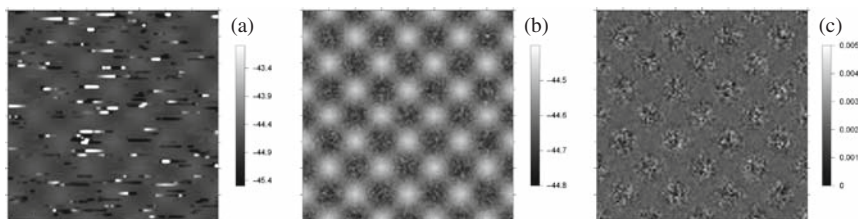


**Fig. 12.5.** Constant height frequency shift images (closest approach of 0.48 nm) of a  $1.7 \times 1.7$  nm area of the MgO (001) surface (a) with the Pd atom diffusing at 110 K (b) 180 K. (c) dissipation image at 180 K, where the units are in eV/cycle

gain) image, where it is possible to see a small dissipation contrast centred around the oxygen sites. This contrast consists of enhanced “noise” and is due to the fact that the Pd rapidly jumping is resulting in many changes to the tip–surface interaction during a single oscillation cycle, so that the force distance–curves on approach and retraction are different (and thus work is done by the tip).

### 12.3.2 H<sub>2</sub>O Adsorbate on CeO<sub>2</sub> (111)

In the example above, we investigated the effect that a rapidly diffusing adatom has on NC-AFM images. In this case, the atom was free to diffuse across the surface, however there are many examples of systems where an adsorbate or surface structure is confined to a small number of accessible states [30]. In this case, the transitions of the system could have a significant effect on the contrast patterns observed.

Recently, experiments have shown images of water adsorbed on the CeO<sub>2</sub> (111) surface [31], which were taken at room temperature. The protrusions assigned to the water adsorbates were triangular in form and observed to encompass three adjacent top oxygen sites. Ab initio calculations were performed that show that a water molecule adsorbs dissociatively on the surface and that the dissociated proton can rotate around the hydroxyl group formed and occupy one of three equivalent states (see Fig. 12.6) [32]. The energy barrier separating these states is calculated to be 0.3 eV, which would result in the proton hopping with a frequency on the order of megahertz at room temperature. This is a qualitatively different behaviour to that displayed in the previous system since the adsorbate is confined to only three equivalent states and is not free to diffuse across the surface.

The force-field of the surface and adsorbed water molecule was determined for atomistic calculations that employed a modified Ceria shell-model potential (the full details of which can be found in [33]) and employed the GULP atomistic simulation code [34]. The tip used for imaging was a hydroxyl terminated MgO tip (in the same orientation as in the previous section), since the tip will have been exposed to water molecules. The fixed time-step KMC

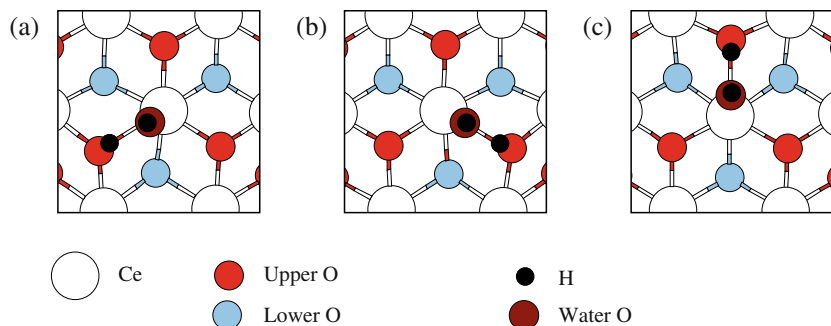


**Fig. 12.6.** Three equivalent accessible configurations of an adsorbed water molecule on the ceria (111) surface [35]

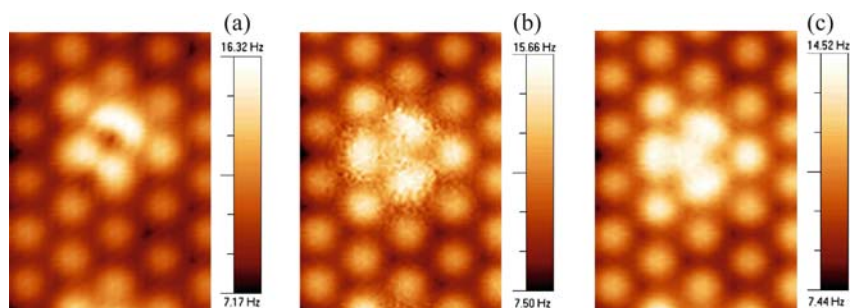


**Fig. 12.7.** Constant height mode images (closest approach of  $4.2 \text{ \AA}$ ) of H<sub>2</sub>O adsorbed on the ceria (111) surface at (a) 4 K, (b) 200 K and (c) 300 K [35]

algorithm was used to determine the thermal transitions of the water molecule between the three configurations. When a jump occurs, the force-field is rotated about the centre of the water molecule by either  $120$  or  $240^\circ$ , i.e., the proton moves either clockwise or anti-clockwise. In these calculations, the barriers are not modified by the presence of the tip, which is an approximation that holds given that the tip does not come too close to the surface.

The parameters for the instrument and cantilever are taken from the corresponding experiment [31]. The resonant frequency of the cantilever is  $71.4 \text{ kHz}$  and the spring constant is  $32 \text{ N/m}$ . The amplitude set-point is set at  $3.75 \text{ nm}$ . As in the previous calculation, a macroscopic van der Waals force is added to the tip-surface interaction with a tip radius of  $1.4 \text{ nm}$  and a Hamaker constant of  $0.4 \text{ eV}$ . The scan is performed in the same way as described in Sect. 12.2, but with a scanning speed of  $3 \text{ nm/s}$ .

Figure 12.7a shows a constant height (frequency shift) image (at  $4.2 \text{ \AA}$ ) of the adsorbed water molecule at 4 K, where no transitions occur throughout the whole image (the structure is that of Fig. 12.6a). The lattice of bright spots in this image correspond to the top oxygen sites in the CeO<sub>2</sub> (111) surface,

and the water molecule appears as an asymmetric protrusion covering three oxygen sites. As the temperature is increased to 200 K the form of the image changes significantly, now the molecule is rotating rapidly with a transition rate of approximately 30 kHz, which is less than the oscillation frequency of the cantilever. The image now has threefold symmetry (Fig. 12.7b). At a temperature of 300 K, the rotation of the molecule is now much more rapid than the cantilever oscillation frequency. The image is similar to that at 200 K, but contains significantly less noise above the molecule.

These calculations indicate that there will be a characteristic “noise” in the frequency shift images due to a rapidly diffusing defect. When defects are immobile, they can be clearly seen in images and may be manipulated by a tip. However, when the temperature is such that defects can make rapid thermally activated hops this can significantly change the appearance of the image.

### 12.3.3 C<sub>60</sub> on Si (001)

We have considered manipulation and thermal motion of adsorbed species which can jump between nearest lattice sites over a small barrier. Here, we shall discuss a different type of a manipulation experiment involving a C<sub>60</sub> molecule adsorbed on the Si(001) surface. The peculiarity of this example is that the molecule is large, spherical and is also strongly bound to the surface.

We note that manipulation of C<sub>60</sub> on this or any other surface has not yet been reported with AFM. However, it was achieved with scanning tunnelling microscopy (STM), both along and across the troughs formed on this surface by Si–Si dimer rows running parallel to each other [36–38]. The process of STM manipulation of C<sub>60</sub> on the Si(001) surface has also been modelled theoretically using *ab initio* DFT calculations [37–39]. These studies show that the most stable adsorption sites of the C<sub>60</sub> on this surface are those in which the molecule makes four chemical bonds with four Si atoms of the surface. This is possible if the molecule is adsorbed either on the dimer row or between two nearest rows (in the trough). There is a large number of possible adsorption configurations [37, 40, 41] with adsorption energies ranging between –0.87 and –2.63 eV. Furthermore, it was shown [37, 42] that the movement of the molecule on the Si(001) surface consists of elementary rolling events in which the molecule pivots over the front two Si–C bonds, while the back two Si–C bonds are broken and then two new Si–C bonds are formed at the front, which bring the molecule to a new adsorption site. Essentially the same rolling mechanism takes place when the molecule is either pushed [38, 39] or pulled [43] by the STM tip.

The barrier for diffusion of C<sub>60</sub> is high,  $\sim 2.5$  eV, and it is the STM tip that pushes (or pulls) the molecule over this barrier (which is reduced by the presence of the tip). Interestingly, it was revealed that the role of the STM tip was not only in reducing the energy barriers for the molecule to roll between two configurations; in fact, it was found that the crucial factor in the STM

manipulation is that the tip keeps a continuous covalent contact with the molecule along the whole manipulation path [38].

Obviously, this type of manipulation would not be possible in NC-AFM experiments due to their very nature: because of the oscillations the tip cannot maintain a continuous contact with the molecule. Therefore, a different mechanism was suggested [44] whereby the molecule thermally diffuses (via rolling) between two neighboring sites, and the role of the tip is in reducing the corresponding energy barrier when the tip is in the proximity of the molecule. In essence, this is the same manipulation mechanism as in the pushing manipulation of a Pd adatom on the Mg (001) surface described earlier.

To investigate the energies of the tip–molecule interaction and the effect of this interaction on the energy barriers for the  $C_{60}$  manipulation in the presence of the tip, we performed a series of calculations using a self-consistent density functional theory-based tight binding (DFTB) code [45, 46].

We considered a series of positions of the molecule along the transition path connecting two stable adsorption sites designated as  $t4c$  and  $t4g$  [41]. In both configurations, the molecule sits in the trough making four C–Si bonds with Si atoms of four Si dimers (see Fig. 12.8c). To model the rolling of the molecule from  $t4c$  to  $t4g$  without the tip (self-diffusion of the molecule), we used a constrained minimization method similar to that used in the earlier ab initio DFT calculations [37, 42]; however, a much bigger surface cell was used. Briefly, a single C atom of the  $C_{60}$  was displaced in small steps along the trough; the displacement coordinate of this atom was fixed, while the rest of the system, apart from the lowest two layers of the Si slab, was allowed to relax, including the other two coordinates of the displaced atom. In this way, the energy barrier in the absence of the tip and the sequence of intermediate configurations for the  $C_{60}$  movement from the configuration  $t4c$  to  $t4g$  were obtained.

To obtain the energy barriers for the  $C_{60}$  manipulation in the presence of the tip, we considered, for each position of the tip, the discrete set of intermediate configurations of the molecule during the transition  $t4c \rightarrow t4g$  as discussed earlier. Single-point energies, without geometry relaxation, were calculated for all these intermediate configurations with a tip present in the system, for a range of tip positions. We used an atomically sharp (111)-oriented Si tip used in the earlier studies of  $C_{60}$  STM manipulation [38, 39, 43] and in other theoretical studies of AFM processes [20, 21, 47]. Two coordinates,  $Y$  and  $Z$ , defined in Fig. 12.8b, determine the tip position relative to the initial  $t4c$  configuration of the molecule. The tip apex height  $Z$  above the top of the  $C_{60}$  ranged between  $-1.6$  and  $2.0 \text{ \AA}$ , and the lateral tip position  $Y$  behind the  $C_{60}$  along the trough (calculated with respect to the centre of mass of the  $C_{60}$  in its starting position) ranged between  $1.0$  and  $6.6 \text{ \AA}$ ; both  $Z$  and  $Y$  were incremented with a step of  $0.2 \text{ \AA}$ .

The relative energies of the  $C_{60}$  movement from the configuration  $t4c$  to  $t4g$  in the presence of the tip are shown in Fig. 12.8a for the lateral tip position

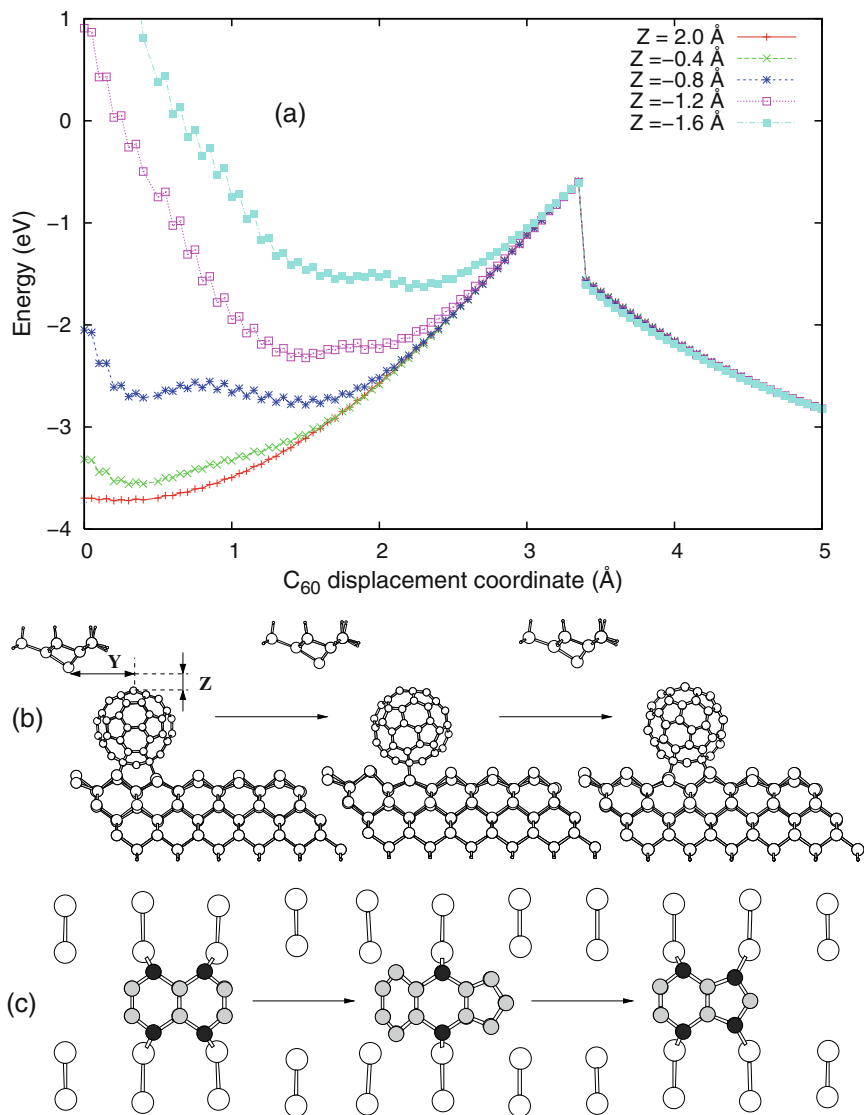


**Fig. 12.8.** (a) Energies of the  $C_{60}$  movement on the Si(001) surface in the presence of the tip at the lateral tip position  $Y = 5$  Å and a range of tip heights  $Z$ . (b) The starting configuration of the  $C_{60}$ , the transition state and the final configuration, together with the definition of the coordinates  $Y$  and  $Z$  of the tip. (c) The top view of the bonding of the molecule to Si atoms of the surface dimers in the three geometries shown in (b); for clarity, only the lower part of the  $C_{60}$  is actually given. In (c), Si atoms are shown with *white circles*, while C atoms with *black* (C atoms bonded to Si) and *grey circles*

$Y = 5 \text{ \AA}$  and a series of heights  $Z$ . The energies are calculated with respect to the isolated  $C_{60}$ , tip and the  $p(2 \times 1)$  reconstructed Si(001) surface. The Figure also shows the initial and final adsorption configurations together with the intermediate transition (pivoting) configuration of the molecule.

We can see that the energies of the  $C_{60}$ -tip-surface system during the movement of the  $C_{60}$  depend strongly on the tip position. While the energy of the second (final) stable configuration and the maximum energy in the transition state (the pivoting point) practically do not depend on the position of the tip (at these points, the molecule is already far from the tip), the energy of the initial configuration and the actual position of the first energy minimum, when the molecule is rotated a little away from the tip, strongly depend on the tip position. The energy goes up if the tip is close to the  $C_{60}$  and down if it is far from it. Thus, the height of the energy barrier for the molecule going from the lowest-energy configuration to the transition state changes depending on the tip position: the barrier becomes smaller if the tip is low above the molecule (small  $Z$ ), and larger, similar to the tip-free case, if the tip is high (large  $Z$ ). Similarly, the  $Y$  position of the tip affects the initial lowest-energy configuration and hence the energy barrier: the barrier is higher if the tip is far from the molecule (large  $Y$  values) and lower if the tip is closer to the molecule.

We stress that these energies are semi-quantitative, since we used an approximate computational approach without relaxation of the system, however, they show the correct trend of energies as a function of the tip position. When the tip is closer to the molecule (small  $Z$  and/or  $Y$ ), barriers become lower and it should be easier for the molecule to overcome them thermally.

We also calculated the force-field acting on the tip for each tip position during its oscillation, for use in explicit simulations of the NC-AFM tip movement. The vertical tip force can be calculated by numerical differentiation of the energy in the energy minima with respect to the tip height,  $Z$ . We find that the forces are repulsive for most of the tip positions near the  $C_{60}$  and become large when the tip is very close to the molecule. As the tip is placed further away from the molecule the interaction becomes weakly attractive and forces tend to zero.

Once the barriers for the molecule to move from one stable site to the other are available for each tip position, it is possible to calculate the corresponding transition rates. Therefore, the entire machinery of the dynamic calculation of the NC-AFM manipulation described in the earlier sections can be used.

For the real-time simulation of the manipulation of  $C_{60}$  by NC-AFM we used the KMC procedure implemented in the VAFM algorithm described earlier. Virtual AFM parameters used in our simulations follow the AFM setup used in an experimental study of the Si(001) surface [48]:  $f_0 = 160 \text{ kHz}$ , spring constant  $k = 40 \text{ N m}^{-1}$ ,  $Q = 10,000$  and the amplitude set point  $A_0 = 100 \text{ \AA}$ . The gain parameters for the amplitude control were  $K_P^A = 0.1 \text{ N m}^{-1}$  and  $K_I^A = 50 \text{ N m}^{-1} \text{ s}^{-1}$ , and for the distance control  $K_P^D = 1 \times 10^{-13} \text{ m s}$  and  $K_I^D = 1 \times 10^{-9} \text{ m}$ . The tip-sample interaction consisted of a short-range

conservative force field obtained from our DFTB calculations as explained earlier, and of a macroscopic van der Waals force. The latter was calculated using a spherical tip model with the tip radius of  $100 \text{ \AA}$  and a Hamaker constant of  $1.165 \text{ eV}$  estimated for the Si–Si interaction [49].

In the VAFM simulations, the vertically oscillating tip initially approaches the substrate from above, a large lateral distance away from the molecule, until the required frequency shift is achieved. Then, the tip is moved laterally towards the  $C_{60}$  along the line that passes through the centre of the molecule above the trough on the Si(001) surface (as a scan line). At each step of the VAFM simulation, the probability of a  $C_{60}$  jump is evaluated using the energy barriers calculated above. If the manipulation is successful, the molecule moves to its next stable adsorption site with the corresponding change of the tip force field and the subsequent reaction of the VAFM which would adjust the tip height in real time. After the first manipulation event, the tip continues to move forward until it comes close enough to the molecule so that it may jump again. This way, a continuous manipulation sequence can be calculated. In these calculations, to simulate each elementary translation of the molecule between two stable sites, we used the same force field and energy barriers as for the  $t4c \rightarrow t4g$  elementary step. This is approximate since the initial and final configurations for each elementary translation may be different [37, 42]. Nevertheless, this approximation will not affect the qualitative picture of the NC-AFM manipulation we are interested in here.

Figure 12.9 shows the distance of closest approach of the tip (defined with respect to the top of the  $C_{60}$  molecule), the frequency shift and the dissipation signal obtained in the VAFM simulations of  $C_{60}$  manipulation at the fixed frequency shift of  $\Delta f = -11 \text{ Hz}$ . The  $C_{60}$  centre of mass is initially at the point which corresponds to  $4.8 \text{ \AA}$  on the horizontal axis of the graph. In Fig. 12.1a, we can see that after the tip has been lowered to the surface (the left part of the topography scan line), it approaches the molecule laterally and images it (the distance of closest approach slightly goes up) until the point indicated by the left arrow, when the molecule jumps. At this point, the tip is very close to the surface. However, after the molecule has jumped from the tip to the right by  $3.8 \text{ \AA}$  (which is the lattice constant of the Si(001) surface),

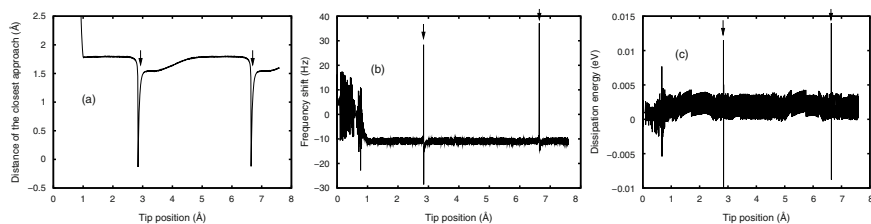


**Fig. 12.9.** (a) Distance of closest approach, (b) frequency shift and (c) dissipation signal during a VAFM scan of  $C_{60}$  on the Si(001) surface at  $\Delta f = -11 \text{ Hz}$  and  $T = 300 \text{ K}$ . The arrows in (a) show the points when manipulation occurs

the feedback system of VAFM raises the tip to the height of  $\sim 1.6 \text{ \AA}$  above the molecule. A new lateral tip approach and imaging of the molecule takes place, until,  $3.8 \text{ \AA}$  later, the tip again approaches the molecule close enough for manipulation to happen (the second arrow). Thus, the distance of closest approach (the topography scan line) has a characteristic shape with the abrupt dips of the tip height at the points of successful manipulation events.

The frequency shift line, Fig. 12.9b, after the initial stabilisation period during  $\sim 1 \text{ \AA}$  of the tip displacement towards the molecule, also shows abrupt peaks at the points of manipulation. There are also peaks in the dissipation signal due to the manipulation events, see Fig. 12.9c, which can also serve to identify the event of successful  $C_{60}$  manipulation by NC-AFM.

We performed VAFM simulations at temperatures  $T = 4, 77, 300,$  and  $600 \text{ K}$  and found that the influence of the temperature on the VAFM scan lines (both the distance of the closest approach, frequency shift and dissipation signal) is small. The  $Y$  coordinate of the tip corresponding to the manipulation events is almost the same at different temperatures. On the other hand, the average value of  $Z$  (the height of the tip) at which manipulation is successful, depends strongly on temperature: lower values of  $Z$  are reached at lower temperatures. This is because lower temperatures require smaller barriers for the manipulation to occur.

To check the reproducibility of the  $C_{60}$  manipulation events, we simulated several scan lines, several hundred  $\text{\AA}$  long each, which resulted in successful manipulation of the molecule every time when the tip moved forward by one lattice constant. Thus, according to our calculations, the manipulation of  $C_{60}$  with an oscillating AFM tip is well reproducible, and the molecule can be manipulated over large distances. In real experiments, such long manipulation sequences may not be achievable due to possible competing processes, for example, the molecule jumping into the neighboring trough or onto the row and therefore getting away from the trajectory of the tip movement.

## 12.4 Discussion

We have presented calculations performed to simulate the NC-AFM imaging and manipulation of three qualitatively different systems, employing a novel multi-scale model of the entire imaging and manipulation process. The first of these involved a single atom adsorbed on an isotropic surface, which can be manipulated at low temperatures and is free to diffuse at higher temperatures. The second example consisted of an adsorbed molecule which was free to rotate on the surface, but confined to a single lattice position. The third example consisted of a very large molecule strongly bound to a surface, which can be manipulated by the tip at close approach. In the first and third examples, it was demonstrated how the adsorbate can be manipulated by the tip. In the first and second examples the effect of thermal motion on images was

determined and it was shown that rapid thermally induced structural changes can change the appearance of an image significantly.

The process of manipulation in this model is described in terms of the modification of the potential energy surface (and hence activation barriers) for the system by the tip at close approach. In both of the two examples of manipulation described earlier, this barrier modification arises due to the repulsive interaction between the tip and the adsorbate. In this case, the adsorbate always moves away from the tip – analogous to “pushing.” However, in other systems manipulation may also occur via a “pulling” mechanism – where an object is manipulated towards the tip through an attractive interaction with the tip apex, as is the case with vacancy manipulation on the MgO (001) surface [29]. In both these cases, manipulation is achieved through modification of the barrier, however the mechanism causing the barrier modification is fundamentally different.

As shown above, our approach can be used to predict optimum protocols for manipulating adsorbed species on surfaces using only the force exerted by an AFM tip apex on the adsorbate. These may guide experimental efforts in achieving control over and adsorbed species: for example, our calculations indicate that manipulation protocols based on scanning provide only limited degree of control that strongly depends on the scanning direction. Choosing the manipulation trajectory and “hitting” the right spot allows a much higher degree of control over the manipulated atom. However, for all the systems, the mechanism for manipulating an object on the atomic scale will always be highly dependent on the exact nature of the termination of the tip apex, as is the case for contrast in images. Quantitative predictions for optimum manipulation protocols will only be accurate so long as the tip used matches that in the actual experiments, which is very difficult to achieve in practise.

The model that has been developed captures both the dynamical evolution of processes occurring in the tip–surface junction as well as the real-time response of the NC-AFM instrument, which represents an extension to the traditional method of modelling NC-AFM images in the conservative regime. This approach provides a reliable “window” into atomic-scale processes during imaging and manipulation, and combined with experimental data may give an important insight into atomic scale surface processes. Experiments exploiting this will significantly broaden the scope of application of the NC-AFM from analyzing static structures to retrieving information about dynamical processes.

## Acknowledgements

We thank J. Polesel Maris and S. Gauthier for their contribution and advice with the Virtual AFM. We would also like to thank M. Watkins, M. Reichling and O. Custance for their advice and valuable discussions.

## References

1. W.A. Hofer, A.S. Foster, A.L. Shluger, *Rev. Mod. Phys.* **75**, 1287 (2003)
2. A.S. Foster, C. Barth, A.L. Shluger, M. Reichling, *Phys. Rev. Lett.* **83**, 2373 (2001)
3. Y. Sugimoto, P. Pou, M. Abe, P. Jelinek, R. Perez, S. Morita, O. Custance, *Nature* **446**, 1287 (2007)
4. F.J. Giessibl, *Rev. Mod. Phys.* **75**, 957 (2003)
5. R. Garcia, R. Perez, *Surf. Sci. Rep.* **47**, 197 (2002)
6. Y. Sugimoto, M. Abe, S. Hirayama, N. Oyabu, O. Custance, S. Morita, *Nat. Mater.* **4**, 156 (2005)
7. Y. Sugimoto, P. Jelinek, P. Pou, M. Abe, S. Morita, R. Perez, O. Custance, *Phys. Rev. Lett.* **98**, 106104 (2007)
8. S. Hirth, F. Ostendorf, M. Reichling, *Nanotechnology* **17**, S148-S154 (2006)
9. L. Kantorovich, *Phys. Rev. B* **64**, 245409 (2001)
10. T. Trevethan, L. Kantorovich, *Surf. Sci.* **540**, 497 (2003)
11. J. Polesel-Maris, S. Gauthier, *J. Appl. Phys.* **97**, 1 (2005)
12. L.N. Kantorovich, J. Polesel-Maris, T. Trevethan, Virtual atomic force microscope simulation code. See EPAPS Document No. E-PRLTAO-98-020702 for the manual and further information.
13. J. Melcher, S.Q. Hu, A. Raman, *Rev. Sci. Instrum.* **79**, 061301 (2008)
14. G. Couturier, R. Boisgard, L. Nony, J.P. Aime, *Rev. Sci. Instrum.* **74**, 2726 (2003)
15. G.H. Enevoldsen, H.P. Pinto, A.S. Foster, M.C.R. Jensen, A. Kuhnle, M. Reichling, W.A. Hofer, J.V. Lauritsen, F. Besenbacher, *Phys. Rev. B* **78**, 045416 (2008)
16. A.S. Foster, A.L. Shluger, R.M. Nieminen, *Nanotechnology* **15**, S60 (2004)
17. R. Hoffmann, A.S. Foster, A. Baratoff, H.J. Hug, H.R. Hidber, H.J. Guntherodt, *Phys. Rev. B* **74**, 245426 (2006)
18. R. Hoffmann R, L.N. Kantorovich, A. Baratoff, H.J. Hug, H.J. Guntherodt, *Phys. Rev. Lett.* **92**, 146103 (2004)
19. A.S. Foster, A.Y. Gal, J.D. Gale, Y.J. Lee, R.M. Nieminen, A.L. Shluger, *Phys. Rev. Lett.* **92**, 036101 (2004)
20. R. Perez, M.C. Payne, I. Štich, K. Terakura, *Phys. Rev. Lett.* **78**, 678 (1997)
21. L. Kantorovich, C. Hobbs, *Phys. Rev. B* **73**, 245420 (2006)
22. L. Kantorovich, *Phys. Rev. B* **75**, 064305 (2007)
23. G.H. Vineyard, *J. Phys. Chem. Solids* **3**, 121 (1957)
24. A.F. Voter, in *Radiation Effects in Solids*, ed. by K.E. Sickafus, E.A. Kotomin, B.P. Uberuaga (Springer, Berlin, 2007)
25. J.A. Venables, L. Giordano, J.H. Harding, *J. Phys.: Condens. Matter* **18**, S411 (2006)
26. Y. Long, N.X. Chen, H.Y. Wang, *J. Phys.: Condens. Matter* **17**, 6149 (2005)
27. L. Kantorovich, T. Trevethan, A. Foster, Self-Consistent Image Force Interaction code, <http://www.cmmf.ucl.ac.uk/lev/codes/SciFi/manual-3-51/index.html>
28. T. Trevethan, M. Watkins, L. Kantorovich, A.L. Shluger, *Phys. Rev. B* **76**, 085414 (2007)
29. T. Trevethan, M. Watkins, A. Shluger, L. Kantorovich, J. Polesel-Maris, S. Gauthier, *Nanotechnology* **17**, 5866 (2006)

30. N. Sasaki, S. Watanabe, M. Tsukada, *Phys. Rev. Lett.* **88**, 046106 (2002)
31. S. Gritschneder, M. Reichling, *Nanotechnology* **18**, 044024 (2007)
32. M. Watkins, A.L. Shluger, *J. Phys. Chem. B* (in press)
33. T.X. Sayle, S.C. Parker, C.R. Catlow, *Surf. Sci.* **316**, 329 (1994)
34. J. Gale, A. Rohl, *Mol. Simul.* **29**, 291 (2003)
35. M. Watkins, T. Trevethan, A.L. Shluger, L.N. Kantorovich, *Phys. Rev. B* **76**, 245421 (2007)
36. P. Moriarty, Y.R. Ma, M.D. Upward, P.H. Beton, *Surf. Sci.* **407**, 27 (1998)
37. N. Martsinovich, C. Hobbs, L. Kantorovich, R.H. Fawcett, M.J. Humphry, D.L. Keeling, P.H. Beton, *Phys. Rev. B* **74**, 085304 (2006)
38. N. Martsinovich, L. Kantorovich, R.H. Fawcett, M.J. Humphry, P.H. Beton, *Small* **4**, 765 (2008)
39. N. Martsinovich, L. Kantorovich, *Nanotechnology* **19**, 235702 (2008)
40. P.D. Godwin, S.D. Kenny, R. Smith, *Surf. Sci.* **529**, 237 (2003)
41. C. Hobbs, L. Kantorovich, J. Gale, *Surf. Sci.* **591**, 45 (2005)
42. D.L. Keeling, M.J. Humphry, R.H. Fawcett, P.H. Beton, C. Hobbs, L. Kantorovich, *Phys. Rev. Lett.* **94**, 146104 (2005)
43. N. Martsinovich, L. Kantorovich, *Phys. Rev. B* **77**, 115429 (2008)
44. N. Martsinovich, L. Kantorovich, in preparation
45. D. Porezag, T. Frauenheim, T. Köhler, G. Seifert, R. Kaschner, *Phys. Rev. B* **51**, 12947 (1995)
46. M. Elstner, D. Porezag, G. Jungnickel, J. Elsner, M. Haugk, T. Frauenheim, S. Suhai, G. Seifert, *Phys. Rev. B* **58**, 7260 (1998)
47. C. Hobbs, L. Kantorovich, *Surf. Sci.* **600**, 551 (2006)
48. T. Uozumi, Y. Tomiyoshi, Y. Sugawara, S. Morita, *Appl. Surf. Sci.* **188**, 279 (2002)
49. T.J. Senden, C.J. Drummond, *Colloids Surf. A* **94**, 29 (1995)